

Effect of nonstoichiometry and amount of additives on the structure of HAp-TiO_y mixtures produced by high-energy fragmentation

S. V. Rempel^{1,2}, K. A. Sergeeva³, H. Schroettner⁴, A. A. Valeeva^{1,2}

¹Institute of Solid State Chemistry UB RAS, 91, Pervomaiskaya st., 620990, Ekaterinburg, Russia

²Ural Federal University named after the first President of Russia B. N. Eltsin, 19, Mira st., 620002, Ekaterinburg, Russia

³Far-Eastern Federal University, 8, Sukhanova st., 690090, Vladivostok, Russia

⁴Institute for Electron Microscopy and Nanoanalysis, Graz University of Technology, Steyrergasse 17/III, A-8010 Graz, Austria

svetlana_rempel@ihim.uran.ru

PACS 81.20.n

DOI 10.17586/2220-8054-2018-9-4-549-557

The nanoparticle sizes in hydroxyapatite (HAp), titanium monoxide (TiO_y) and HAp-TiO_y mixtures ($y = 0.92; 1.23$) have been studied by XRD and HRTEM techniques as a function of milling time. It was established that the high-energy milling does not lead to a considerable decrease in the particle size and to a variation in the HAp crystal lattice parameters, but it promotes 4-fold reduction of microstrains. It was shown that the dependence of the average size of crystal and structural parameters on the milling time for the HAp-TiO_y mixtures is similar to that of initial HAp. The coherent scattering region of HAp does not depend on stoichiometry and TiO_y content in the mixture and is $\sim 15 \pm 5$ nm after milling for 480 min.

Keywords: titanium monoxide, hydroxyapatite, milling, mixtures, crystal structure, microstructure, phase composition.

Received: 28 May 2018

Revised: 13 July 2018

1. Introduction

High-energy milling in a planetary ball mill is a common technique of producing nanomaterials [1]. This technique can be also used for creating of composite materials for medicine since nanoceramics and mixtures have some advantages over macro- and microcrystalline materials. For example, HAp ceramics exhibits an enhanced ability to osteosynthesis and adhesion of osteoblasts compared with microstructured ceramics [2–6]. The shape and aspect ratio of nanoparticles are also of much importance for creating favorable conditions for adhesion [2]. In recent years, the nanostructured calcium orthophosphates, in particular, HAp become an active research field in materials synthesis [7–11]. High-energy milling can be a convenient method of unification of nanoparticles of different shape obtained by different techniques. However, the processes occurring during fragmentation and mixing of materials having essentially different properties require a detailed study. So, the Vickers microhardness of the initial components of the composite nanomaterial HAp/TiO [12] differs on several times and is 138 and 992 MPa for HAp and TiO, respectively. In that case, mechanosynthesis, destruction of a softer material by a harder material, and the appearance of excess microstrains that can affect the properties of the final material etc. may take place. The aim of this work is to study in detail the effect of high-energy fragmentation on the microstructure, phase composition, and microstresses of materials and initial components of HAp/TiO_y mixture, as well as the effect of nonstoichiometry of TiO_y additives on these properties.

2. Experimental

Stoichiometric HAp and microcrystalline TiO_y were produced using the techniques described in works [13–15]. Nanocrystalline HAp, TiO_y powders ($y = 0.92$ and 1.23) and their mixtures were produced by high-energy milling in a Retsch PM 200 planetary ball mill using Y₂O₃-stabilized ZrO₂ grinding media and vials. The ball-to-powder weight ratio was 10 : 1. The high-energy milling conditions were as follows: milling time of 15, 30, 60, 120, 240, and 480 min; rotation direction reversed every 15 min; interval between direction reversals, 5 s; rotation speed of the disk supporting the grinding vials, 500 rpm. Note that the milled nanopowders contain impurities of Y₂O₃-stabilized ZrO₂ ($\sim 2 - 3$ %) and carbon since milling was performed in Y₂O₃-stabilized ZrO₂ grinding media and vials with the use of isopropanol [16].

The morphology of the initial microcrystalline powders and mixtures after milling was studied by high-resolution scanning electron microscopy (SEM) on a ZEISS Ultra 55 microscope. The lens-to-sample distance and

the accelerating voltage were 3.4 – 4.0 mm and 5 keV, respectively. The beam width varied from 1 to 115 μm depending on magnification.

The structure and microstructure of HAp was determined using high-resolution transmission electron microscopy (HRTEM) on a JEM 2010 electron microscope (JEOL, Japan) with accelerating voltage 200 kV. To perform electron microscopy studies, the particles were placed into alcohol and were applied on carbon substrates (biological adhesive) (diameter of holes $\sim 1 \mu\text{m}$) fixed on copper or molybdenum networks. The particles were applied by means of ultrasonic disperser providing a uniform distribution of particles on the substrate surface. After the particles on the carbon substrate and network were removed from the alcohol, it was evaporated.

The X-ray diffraction (XRD) studies of the powders were performed in $\text{CuK}\alpha_1$ -radiation on a STADI-P automatic diffractometer (STOE, Germany) in the Bragg–Brentano geometry by stepwise scanning with $\Delta(2\theta) = 0.02^\circ$ in the angle interval from 10 to 120° with a high degree of statistics. Polycrystalline silicon ($a = 543.07 \text{ pm}$) was used as external standard. Phase analysis of the XRD pattern was performed using Powder Cell 2.4 program. For phase identification the powder standards database ICDD PDF2 (ICDD, USA, Release 2009) was used.

Diffraction line profiles were analyzed by fitting with pseudo-Voigt functions of the form:

$$V(\theta) = ca \left[1 + \frac{(\theta - \theta_0)^2}{\theta_L^2} \right]^{-1} + (1 - c)a \exp \left[-\frac{(\theta - \theta_0)^2}{2\theta_G^2} \right], \quad (1)$$

where c is the relative contribution of the Lorentzian function to the total reflection intensity; θ_L and θ_G are the Lorentz and Gauss profile parameters, respectively; a is a normalizing intensity factor; and θ_0 is the function and reflection maximum position.

The numerical analysis of X-ray diffraction patterns was performed using the technique [11, 12, 17, 18]; it revealed that the powders are homogeneous and single-phase. Therefore, the average size of the coherent scattering regions was determined as [19, 20]:

$$D = K_{hkl} \cdot \frac{\lambda}{\cos \theta} \cdot \beta(2\theta) \equiv K_{hkl} \cdot \frac{\lambda}{2} \cdot \cos \theta \cdot \beta(\theta), \quad (2)$$

where K_{hkl} is the James coefficient, and $\beta(2\theta)$ is the broadening. The diffraction reflection broadening $\beta(2\theta) \equiv 2\beta(\theta)$ was determined as:

$$\beta(2\theta) = \sqrt{\text{FWHM}_{\text{exp}}^2 - \text{FWHM}_{\text{R}}^2}. \quad (3)$$

The instrumental broadening (the resolution function of the diffractometer) was determined in a special diffraction experiment with a standard powder of lanthanum hexaboride LaB_6 (NIST Standard Reference Powder 660a) with cubic lattice spacing $a_{\text{cub}} = 415.69 \text{ pm}$ and particle size of $\sim 10 \mu\text{m}$. The resolution function of the diffractometer, determined with lanthanum hexaboride, had the following parameters: $u = 0.0058$, $v = -0.0046$, $w = 0.0101$.

The particle size and microstrain contributions to the reflection broadening were determined by the Williamson–Hall technique [21, 22]. The reduced broadening was calculated by the formula

$$\beta^*(2\theta) = \beta(2\theta) \cos \theta / \lambda. \quad (4)$$

The experimental broadening $\beta(2\theta)$ is a superposition of particle size β_s and strain β_d broadening:

$$\beta = \sqrt{\beta_s^2 + \beta_d^2}. \quad (5)$$

The size of nanoparticle coincides with the coherent scattering region (CSR). The CSR size was determined as:

$$\langle D \rangle = 1/\beta^*(2\theta = 0). \quad (6)$$

The size of nanoparticle was determined by extrapolating $\beta^*(s)$ to $s = 0$, and the lattice microstrain was found from the slope of the resultant straight line. Lattice strain $\varepsilon = \Delta d/d_0$, where d_0 is the average interplanar spacing and Δd is its deviation, leads to a strain-induced diffraction line broadening $\beta d(2\theta) = 2\varepsilon \tan \theta$.

The dependence of the CSR and the volume fraction of nanoparticles on the milling time were described by the relations proposed in [23]:

$$D(\tau) = \frac{D_0 - D_{\text{min}}}{1 + b\tau} + D_{\text{min}}, \quad (7)$$

$$V(\tau) = \frac{a}{1 - \exp(-\tau/\tau_0)}, \quad (8)$$

where D_0 is the initial particle size before milling; D_{min} is the minimal particle size achieved by milling; b is the coefficient related to softness of material; a is the volume contribution of nanodimensional fraction; and τ is the time of milling.

For more accurate determination of the compounds' crystal lattice parameters, the Nelson–Riley extrapolation function was used:

$$0.5 \left[\frac{\cos^2 \theta}{\sin \theta} + \frac{\cos^2 \theta}{\theta} \right], \quad (9)$$

where θ is the scattering angle.

3. Results and discussion

The analysis of the X-ray diffraction patterns of the initial and milled HAp showed that all powders are homogeneous and single-phase. The crystal structure of HAp belongs to the hexagonal system (sp. gr. $P 63/m$). As the milling time increases, a small broadening of diffraction reflections occurs and their intensity lowers (Fig. 1). The position of reflections remains unchanged within the accuracy of the experiment. After milling, the type and crystal lattice symmetry of the HAp are retained. When 10 and 20 wt.% titanium monoxide are introduced into HAp, additional diffraction reflections corresponding to $(111)_{B1}$, $(200)_{B1}$ and $(202)_{B1}$ reflections are observed on the HAp X-ray diffraction patterns (Fig. 1). These reflections exhibit a high intensity. The considerable widths of the $(200)_{B1}$ and $(202)_{B1}$ reflections are due to the overlapping with the HAp diffraction reflections.

According to analysis of X-ray patterns, the average CSR size of initial HAp is 20 ± 5 nm. As a result of milling, the particle size was decreased to 13 ± 5 nm (Fig. 2).

The parameters of the model curve (formula 7), which was used for data approximation, are $D_0 = 20$ nm, $b = 0.02$ and $D_{\min} = 13$ nm. As the time of milling increases, the microstrain value decreases (Fig. 2) by hyperbolic function $y = y_0 + a \exp(-kx)$ with parameters $y_0 = 0.10$, $a = 0.30$ and $k = 0.04$.

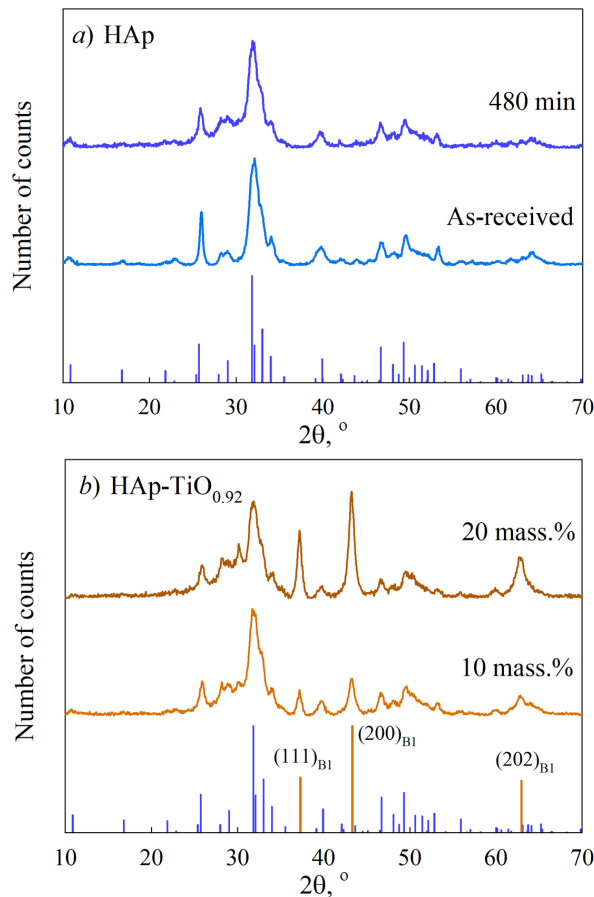


FIG. 1. The X-ray diffraction patterns of HAp powders (a) and HAp-TiO_{0.92} mixture (b) vs. the milling time and the content of titanium monoxide. The position and intensity of diffraction peaks of hydroxyapatite with unit cell parameters $a = 940.0$ pm and $c = 693.0$ pm (card 98-008-6843) and titanium monoxide with the disordered cubic cell parameter $a = 418.5$ pm are given below

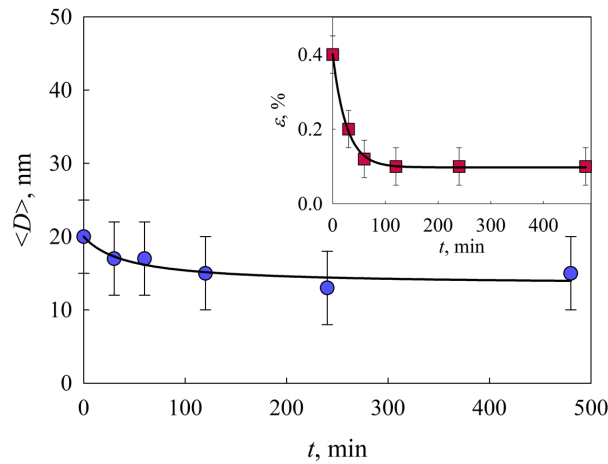


FIG. 2. The CSR size and the HAp crystal lattice microstrain value (inset) as functions of the milling time

The dependences of the CSR size and the volume fraction of nanoparticles on the time of milling for sub- and superstoichiometric compositions of titanium monoxide are shown in Fig. 3. Both materials are characterized by the presence of microparticles even after 480 min milling.

The performed calculations revealed that the unit cell parameters a and c of HAp powders change within the computational error as the milling duration increases. The parameter a changes insignificantly, and the parameter c increases monotonically. The lattice parameter of titanium monoxide changes little, if at all, and the cubic structure remains stable after milling for 480 min. More detailed data on the structural parameters of HAp and TiO_y powders are presented in Table 1.

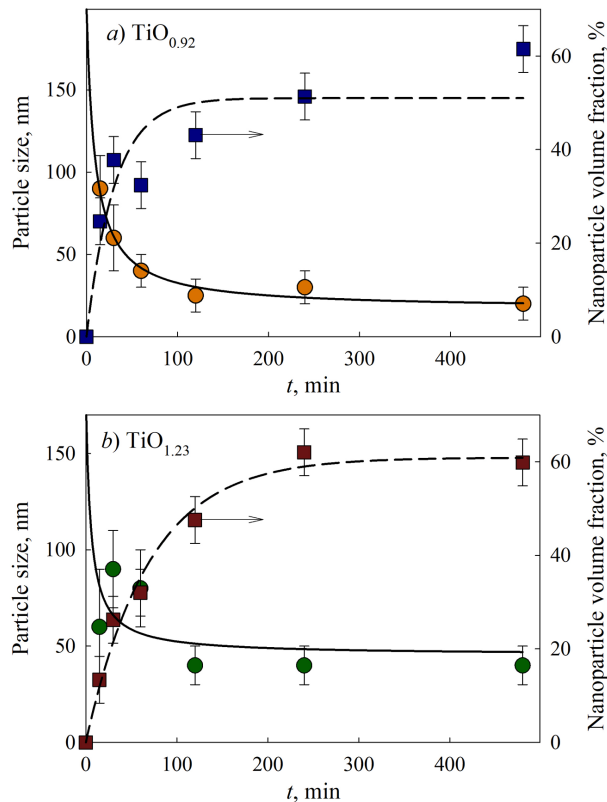


FIG. 3. The CSR size and the volume fraction of TiO_y ($y = 0.92$ (a); 1.23 (b)) powder nanoparticles as functions of the milling time

TABLE 1. The properties of initial and milled HAp and titanium monoxide powders

Compound	Milling time, min	Lattice constant <i>a</i> and <i>c</i> , pm (± 1 nm)	Crystal size $\langle D \rangle > \pm 5$ nm	Volume fraction of nanoparticles, %	Microstrains, %
Initial HAp	0	<i>a</i> = 941.5, <i>c</i> = 688.6	20	100	0.4
	30	<i>a</i> = 941.7, <i>c</i> = 689.0	17	100	0.2
	60	<i>a</i> = 941.7, <i>c</i> = 689.3	17	100	0.12
	120	<i>a</i> = 942.0, <i>c</i> = 689.4	15	100	0.1
	240	<i>a</i> = 941.5, <i>c</i> = 689.5	13	100	0.1
	480	<i>a</i> = 941.5, <i>c</i> = 691.1	15	100	0.1
Initial TiO _{0.92}	0	<i>a</i> = 418.5	200	0	0.0013
	30	<i>a</i> = 418.5	60	37	0.27
	60	<i>a</i> = 418.5	40	32	0.39
	120	<i>a</i> = 418.5	25	43	0.41
	240	<i>a</i> = 418.6	30	51	0.65
	480	<i>a</i> = 418.5	20	61	0.73
Initial TiO _{1.23}	0	<i>a</i> = 416.9	180	0	0.0015
	30	<i>a</i> = 416.9	90	16	0.27
	60	<i>a</i> = 416.9	80	32	0.41
	120	<i>a</i> = 416.9	40	47	0.47
	240	<i>a</i> = 416.8	40	62	0.59
	480	<i>a</i> = 416.9	40	60	0.85

Analysis of the X-ray diffraction patterns of HAp/TiO_y mixtures demonstrated that the dependence of the average CSR size and structural parameters on the time of milling is similar to that for the initial HAp. Note that the size of CSR of mixture components corresponds within experimental error to the values for milled HAp and TiO_y (Table 2). Moreover, the CSR size of HAp does not depend on stoichiometry and the content of TiO_y in mixtures and is $\sim 15 \pm 5$ nm.

TABLE 2. The properties of mixtures after 480 min milling

Mixture	HAp-TiO _{0.92} (10 mass.%)		HAp-TiO _{0.92} (20 mass.%)		HAp-TiO _{1.23} (10 mass.%)		HAp-TiO _{1.23} (20 mass.%)	
	HAp	TiO _{0.92}	HAp	TiO _{0.92}	HAp	TiO _{1.23}	HAp	TiO _{1.23}
Crystal size $\langle D \rangle \pm 5$, nm	18	12	16	12	16	30	15	13
Microstrains, %	0.2	0.9	0.03	0.9	0.05	0.35	0.06	0.9
Lattice constant <i>a</i> and <i>c</i> , pm (± 1)	<i>a</i> = 941.6, <i>c</i> = 688.9	<i>a</i> = 417.8	<i>a</i> = 941.2, <i>c</i> = 690.5	<i>a</i> = 418.1	<i>a</i> = 941.2, <i>c</i> = 687.3	<i>a</i> = 416.7	<i>a</i> = 942.2, <i>c</i> = 692.5	<i>a</i> = 416.8

The lowest crystal lattice microstrain value of HAp in HAp-TiO_y mixture corresponds to substoichiometric composition TiO_{0.92} and amounts to 0.03 % (Table 2). When mixtures are milled in the presence of additives, the HAp crystal lattice parameters change nonmonotonically (Fig. 4). The changes depend on both the amount and nonstoichiometry of the additives.

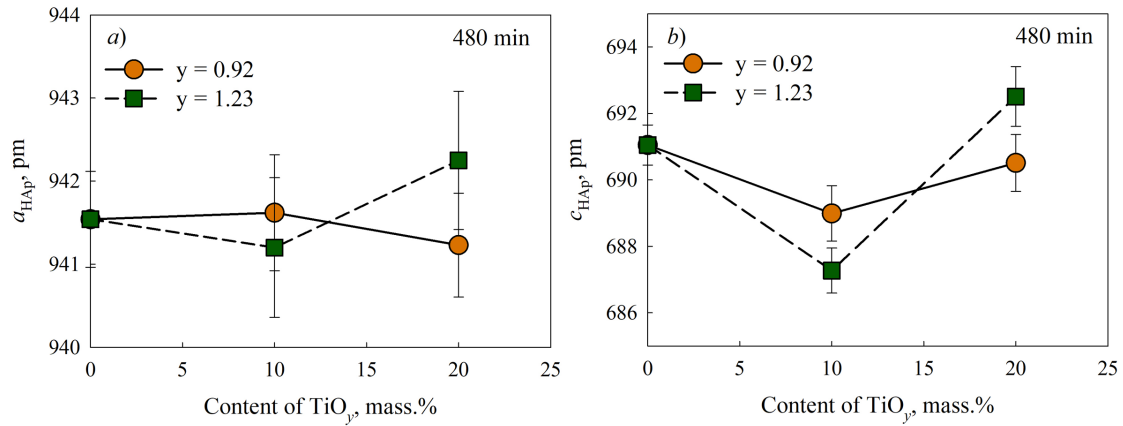


FIG. 4. The HAp crystal lattice parameters a and c as functions of the titanium monoxide TiO_y content ($y = 0.92$ (a); 1.23 (b)) with different stoichiometry

According to the SEM data, the initial HAp contains mainly cylindrical nanoparticles (Fig. 5) to 250 nm in length and ~ 20 nm in diameter. Analysis of the SEM data of milled HAp showed that such nanoparticles were not observed any longer. According to the HRTEM data, the sample consists of HAp particles (card# 98-008-6843); cylindrical particles of the length to 100 nm (Fig. 6) are observed on the surface of larger particles. The CSR size also decreases, but not so considerably. Taking into account the X-ray diffraction data, it can be supposed that the initial cylindrical HAp nanoparticles are polycrystals growing during synthesis mainly along the crystallographic direction c . During milling, both fragmentation of nanoparticles and reduction of their constituent blocks predominately along the a direction take place.

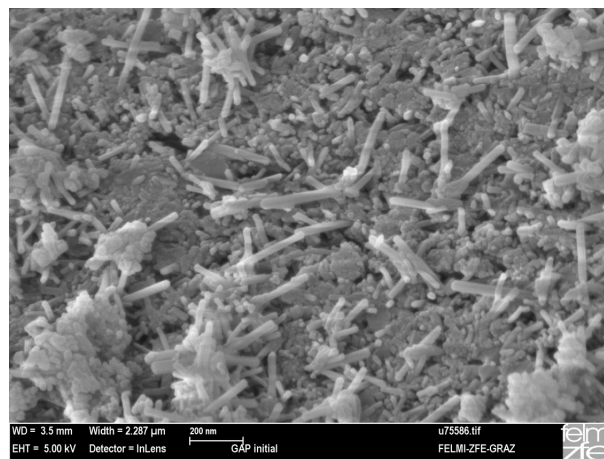


FIG. 5. The microphotographs of the initial HAp powder before fragmentation, SEM

Figures 7 and 8 display the microphotographs of microcrystalline monoxides (sub- and superstoichiometric) and nanocrystalline TiO_y after milling for 480 min. After milling, the TiO_y nanopowders are represented by agglomerates to 200 – 250 nm in size, consisting of bound together nanoparticles with a size of about 20 nm.

It is interesting that after milling of HAp and TiO_y nanoparticles in a planetary ball mill for 480 min, the morphology of the mixture becomes similar to the morphology of nanocrystalline TiO_y [18,23] (Fig. 9). Owing to additives, the particles of the mixture acquire a flattened shape that facilitates the compaction and promotes the adhesion of cells. The morphology of the powders does not depend on the stoichiometry of additives.

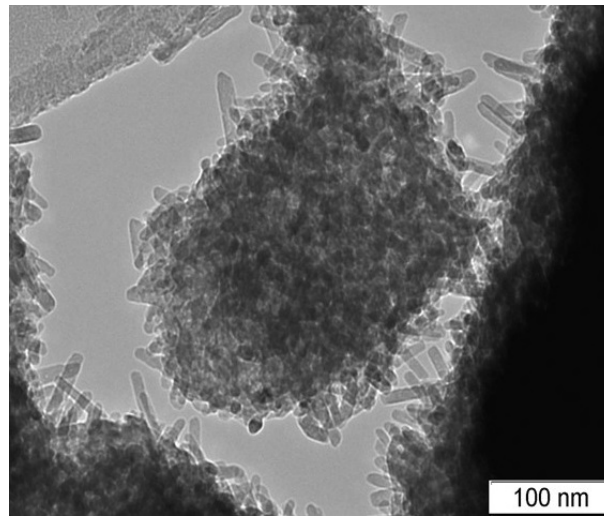


FIG. 6. The microphotograph of HAp powder nanoparticles after 480 min milling, HRTEM

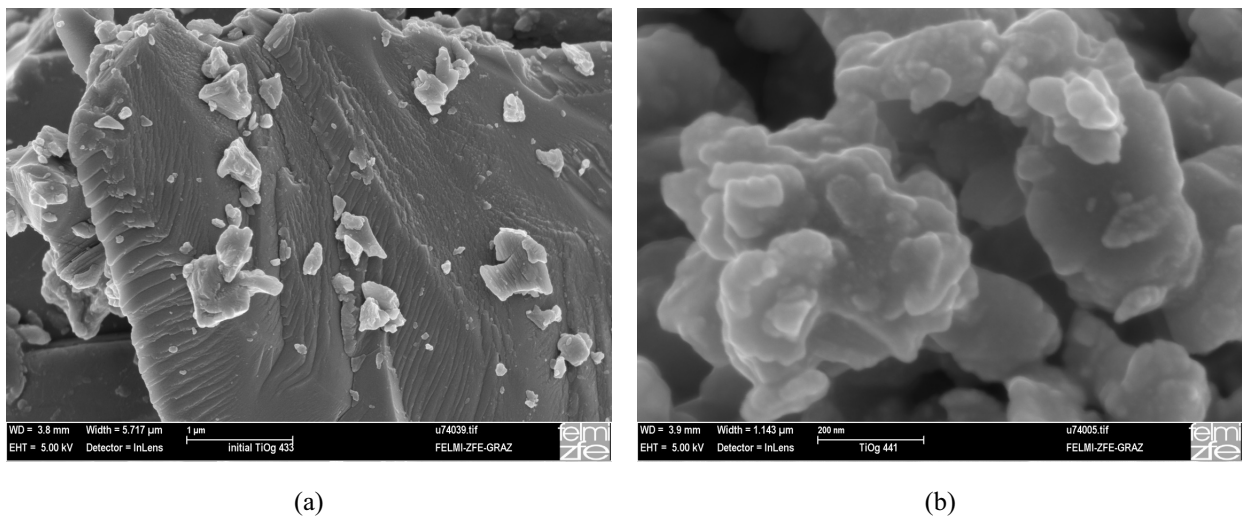


FIG. 7. The microphotographs of substoichiometric titanium monoxide TiO_{0.92}: a) initial, microcrystalline; b) after 480 min high-energy milling, SEM

4. Conclusion

The structural and morphological studies of HAp, TiO_y ($y = 0.92; 1.23$) nanopowders and their mixtures produced by high-energy milling have been carried out. It was established that after the fragmentation the crystal structure of HAp is retained. The high-energy milling does not lead to a variation in the HAp crystal lattice parameters, promoting however a 4-fold reduction in microstrain. The dependence of the CSR size on the HAp milling time is reliably described by the function proposed earlier for titanium monoxide. This hyperbolic function can be also applied to other nonstoichiometric oxides and carbides of transition metals.

It is shown that for HAp/TiO_y mixtures ($y = 0.92; 1.23$) the dependence of the average CSR size and structural parameters on the milling time is similar in many respects to that for initial HAp. The HAp CSR size does not depend on the stoichiometry and content of TiO_y in mixtures and is $\sim 15 \pm 5$ nm upon 480 min milling. The least microstrain value of HAp crystal lattice in HAp-TiO_y nanocomposite corresponds to the substoichiometric composition TiO_{0.92}.

After milling, the nanopowder mixtures acquire the morphology of TiO_y nanopowders, which is favorable for compaction and adhesion of cells during further application.

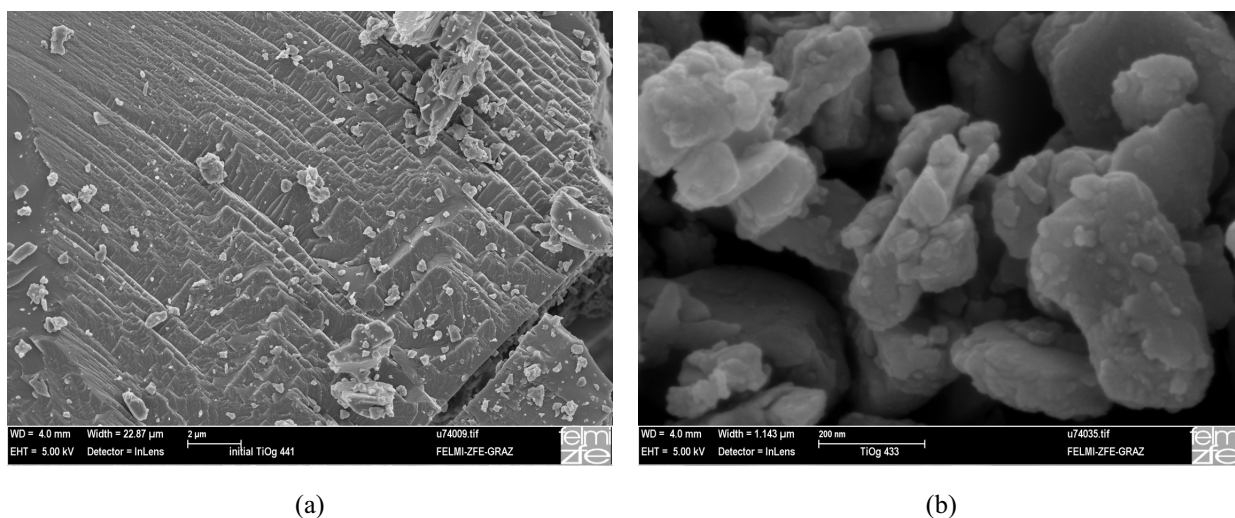


FIG. 8. The microphotographs of superstoichiometric titanium monoxide $\text{TiO}_{1.23}$: a) initial, microcrystalline; b) after 480 min high-energy milling, SEM

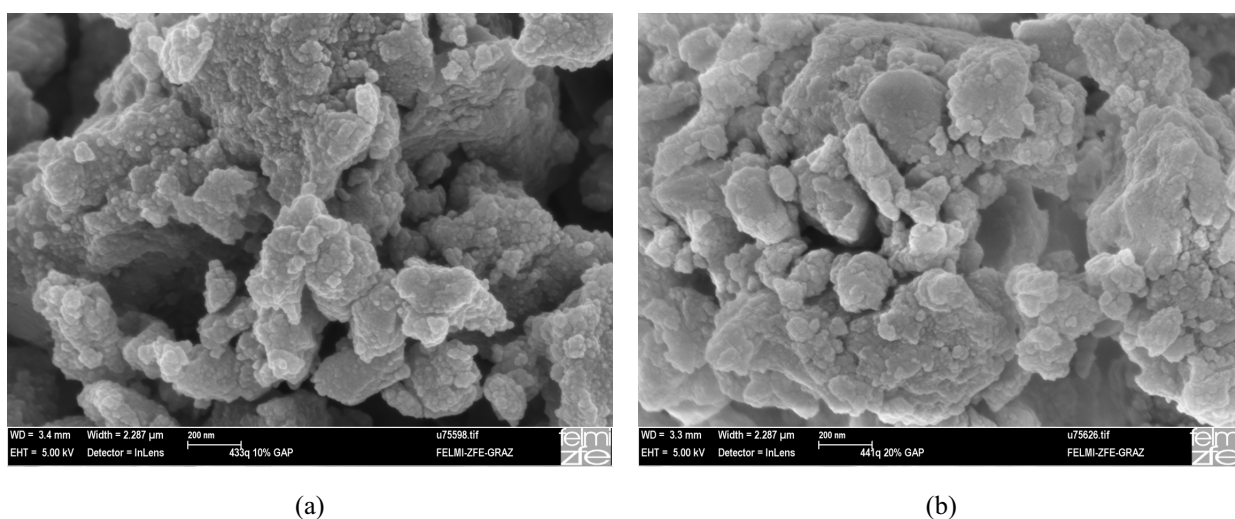


FIG. 9. The microphotographs of powder mixtures after 480 min high-energy milling: a) HAp/ $\text{TiO}_{0.92}$; b) HAp/ $\text{TiO}_{1.23}$, SEM

Thus, the high-energy milling does not change the crystal structure of initial nanopowders, it decreases microstrains and unifies the morphology. The stoichiometry of TiO_y additives has no considerable effect on the CSR size of the mixtures.

Acknowledgements

The work was carried out at the Institute of Solid State Chemistry UB RAS with financial support from the Russian Science Foundation (Project 14-23-00025). The authors are grateful to E. A. Bogdanova for the synthesis of HAp powders and E. Yu. Gerasimov for HRTEM experiment.

References

- [1] Rempel A.A. Nanotechnologies. Properties and applications of nanostructured materials. *Russian Chemical Reviews*, 2007, **76**, P. 435–461.
- [2] Okada M., Matsumoto T. Japanese Synthesis and modification of apatite nanoparticles for use in dental and medical applications. *Dental Science Review*, 2015, **51**, P. 85–95.
- [3] Okada M., Furuzono T., Hydroxylapatite nanoparticles: fabrication methods and medical applications. *Sci. Technol. Adv. Mater.*, 2012, **13** (064103), P. 1–14.
- [4] Webster T.J., Ergun C., et al. Enhanced osteoclast-like cell functions on nanophase ceramics. *Biomaterials*, 2001, **22**, P. 1327–1333.

- [5] Balasundaram G., Sato M., Webster T.J. Using hydroxyapatite nanoparticles and decreased crystallinity to promote osteoblast adhesion similar to functionalizing with RGD. *Biomaterials*, 2006, **27**, P. 2798–2805.
- [6] Sun W., Chu C., Wang J., Zhao H. Comparison of periodontal ligament cells responses to dense and nanophase hydroxyapatite. *J. Mater. Sci. Mater. Med.*, 2007, **18**, P. 677–683.
- [7] Wen Z., Wang Z., et al. Manipulation of partially oriented hydroxyapatite building blocks to form flowerlike bundles without acid-base regulation. *Colloids and Surfaces B: Biointerfaces*, 2016, **142**, P. 74–80.
- [8] Terraschke H., Rothe M., et al. In situ luminescence analysis: a new light on monitoring calcium phosphate phase transitions. *Inorg. Chem. Front.*, 2017, **4**, P. 1157–1165.
- [9] Shkir M., Kilany M., Yahia I.S. Facile microwave-assisted synthesis of tungsten-doped hydroxyapatite nanorods: A systematic structural, morphological, dielectric, radiation and microbial activity studies. *Ceramics International*, 2017, **43**, P. 14923–14931.
- [10] Abutalib M.M., Yahia I.S. Novel and facile microwave-assisted synthesis of Mo-doped hydroxyapatite nanorods: Characterization, gamma absorption coefficient, and bioactivity. *Materials Science and Engineering C*, 2017, **78**, P. 1093–1100.
- [11] Hu S., Jia F., et al. Ferroelectric polarization of hydroxyapatite from density functional theory. *RSC Adv.*, 2017, **7**, P. 21375–21379.
- [12] Rempel S.V., Valeeva A., et al. Vacuum-made nanocomposite of low-temperature hydroxyapatite and hard nonstoichiometric titanium monoxide with enhanced mechanical properties. *Mendeleev Commun.*, 2016, **26**, P. 543–545.
- [13] Rempel S.V., Bogdanova E., et al. Microhardness and phase composition of TiO_y/hydroxyapatite nanocomposites synthesized under low-temperature annealing conditions. *Inorganic Materials*, 2016, **52** (5), P. 476–482.
- [14] Valeeva A.A., Rempel A.A., Gusev A.I. Ordering of Cubic Titanium Monoxide into Monoclinic Ti₅O₅. *Inorganic Materials*, 2001, **37**, P. 603–613.
- [15] Valeeva A.A., Rempel S.V., Schroettner H., Rempel A.A. Influence of the degree of order and nonstoichiometry on the microstructure and microhardness of titanium monoxide. *Inorganic Materials*, 2017, **53**, P. 1174–1179.
- [16] Valeeva A.A., Petrovykh K.A., Schroettner H., Rempel A.A. Effect of stoichiometry on the size of titanium monoxide nanoparticles produced by fragmentation. *Inorganic Materials*, 2015, **51**, P. 1132–1137.
- [17] Rempel A.A., Rempel S.V., Gusev A.I. Quantitative assessment of homogeneity of nonstoichiometric compounds. *Doklady Physical Chemistry*, 1999, **369**, P. 321–325.
- [18] Rempel A.A., Gusev A.I. Preparation of disordered and ordered highly nonstoichiometric carbides and evaluation of their homogeneity. *Physics of the Solid State*, 2000, **42**, P. 1280–1286.
- [19] Warren B.E. *X-Ray Diffraction*. Dover Publications, New York, 1990. 381 p.
- [20] James R. *Optical principles of X-Ray diffraction*. Foreign Literature Publishing House, Moscow, 1950, 574 p.
- [21] Hall W.H. X-ray line broadening in metals. *Proc. Phys. Soc. A*, 1949, **62**, P. 741–743.
- [22] Hall W.H., Williamson G.K. The diffraction pattern of cold worked metals: I. The nature of extinction. *Proc. Phys. Soc. B*, 1951, **64**, P. 937–946.
- [23] Valeeva A.A., Schroettner H., Rempel A.A. Fragmentation of disordered titanium monoxide of stoichiometric composition TiO. *Russian Chemical Bulletin*, 2014, **63**, P. 2729–2732.